

AUTOMATED SEA ICE CLASSIFICATION USING SENTINEL-1 IMAGERY

Jeong-Won Park¹, Anton Korosov², Mohamed Babiker², Hyun-Cheol Kim¹

¹Korea Polar Research Institute, Incheon, South Korea

²Nansen Environmental and Remote Sensing Center, Bergen, Norway

ABSTRACT

Sentinel-1A and 1B operate in Extra Wide swath dual-polarization mode over the Arctic Seas, and the two-satellite constellation provides the most frequent SAR observation of the Arctic sea ice ever. However, the use of Sentinel-1 for sea ice classification has not been popular because of relatively higher level of system noise and radiometric calibration issues. By taking advantage of our recent development on Sentinel-1 image noise correction, we suggest a fully automated SAR image-based sea ice classification scheme which can provide a potential near-real time services of sea ice charting. The denoised images are processed into texture features and a machine learning-based classifier is trained by feeding digitized ice charts. The use of ice chart rather than manually classified reference image makes enable an automated training which minimizes the effects from biased human decision. The resulting classifier was tested over the Fram Strait area for an extensive dataset of Sentinel-1 constellation acquired from October 2017 to May 2018. The classification results are shown in comparison with the ice charts, and the feasibility of the ice chart-fed automated classifier is discussed.

Index Terms— synthetic aperture radar, Sentinel-1, sea ice, classification

1. INTRODUCTION

Wide swath SAR observation from several spaceborne SAR missions played an important role in studying global ocean and ice-covered polar region. Sentinel-1A and 1B are producing dual-polarization observation data with the highest temporal resolution ever. The cross-polarization is known to be more sensitive to the difference in scattering from sea ice and open water than the co-polarization, and the combination of HH- and HV-polarizations has been widely used for ice edge detection and ice type classification. However, the majority of the recent ice classification algorithms were developed using RADARSAT-2 ScanSAR images [1-3] which has different sensor characteristics from Sentinel-1 TOPSAR, and the use of Sentinel-1 for the same purpose is very limited in literature. The main drawback of applying existing algorithms to Sentinel-1 data is the relatively higher level of thermal noise contamination and its propagation to image textures.

For a proper use of dense time-series, radiometric properties must be well calibrated. Thermal noise is often neglected in many applications but is impacting seriously the utility of dual-polarization SAR data. Sentinel-1 TOPSAR image intensity is disturbed by the thermal noise particularly in cross-polarization channel. Although the European Space Agency (ESA) provides calibrated noise vectors for noise power subtraction, residual noise contribution is significant considering relatively narrow backscattering distribution of the cross-polarization channel. In our previous study in [4], a new denoising method with azimuth de-scalloping, noise scaling, and inter-swath power balancing was developed and showed improved performance in various SAR intensity-based applications. Furthermore, when it came to texture-based image classification, we suggested a correction method for textural noise [5] which distorts local statistics thus degrades texture information in Sentinel-1 GRD product. Fig. 1 shows a comparison between two different denoised images and their corresponding textures. The four left panels are from the standard ESA denoising which is a simple subtraction of the annotated noise vectors. There are notable offsets in entropy values between the first and second subswaths for both polarizations, while such artifacts are not seen in the four right panel images processed with our denoising method. Although here we show entropy images only, other texture features show similar patterns originated from the thermal noise and a potentially systematic fault in radiometric calibration. This is probably the reason why the first subswath was abandoned in some literatures like [6,7].

In this work, we present a fully automated Sentinel-1 image-based sea ice classification algorithm which takes an advantage of our denoising method. The noise corrected dual-polarization images are processed into image textures that capture sea ice features in various spatial scale, and they are used for training a machine learning-based classifier by relating with ice charts published by operational ice services. The use of existing ice charts has dual purposes: i) automatization of classifier training, and ii) minimization of human error. Once the classifier is generated, the accuracy and computational complexity are assessed to see if it enables near-real time operation with sufficiently short time delay from the image acquisition.

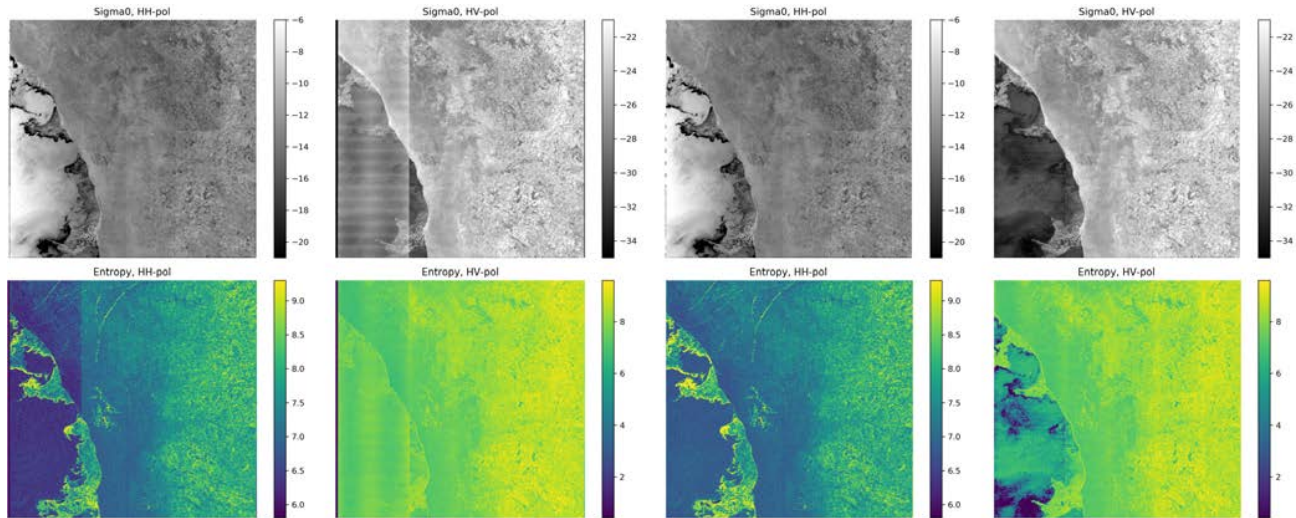


Fig. 1. Sigma nought and entropy images processed using the denoised results by applying the standard ESA method (left four panels) and the NERSC method in [4,5] (right four panels).

2. DATA SET

The region of interest is the Fram Strait where various sea ice types coexists because of the highly strong ice export.

2.1. Sea ice charts

For developing a fully automated classifier, the training scheme also needs to be automated by feeding periodically updated references. At the moment, there are several ice charts published by different ice services. Among them, AARI (Arctic and Antarctic Research Institute, Russia) and NIC (National Ice Center, USA) publishes weekly updated ice charts with global coverage. Both ice charts follow the WMO standards for sea ice information and are provided in the SIGRID-3 format [8]. In this study, we use the AARI ice chart only, but the processing scheme can also be applied for the NIC ice chart in the same way.

2.2. Sentinel-1 EW mode imagery

The Sentinel-1 constellation observes the whole Arctic in Extra Wide (EW) swath mode with dual-polarization (HH/HV). Effective temporal resolution is less than 1-day and the number of daily production is more than 150 scenes. In this study, we use GRDM (Ground Range Detected, Medium resolution) products which have 400 km swath width with 40 m pixel spacing. From October 2017 to May 2018, nearly two thousand scenes were acquired over the study area, and they are freely available from the Copernicus Open Access Hub (<https://scihub.copernicus.eu>).

3. METHODS

3.1. Ice chart processing

In ice charts, each polygon contains various attributes including ice concentration, ice form, and stage of development. The ice type in this study refers to the stage of development (SoD). Since the ice characteristics are

described as a mixture of different ice types with their corresponding partial concentrations while our classifier will not perform multi-label classification, it is necessary to assign each of the polygons to representative specific ice types and to reproject them into the SAR image geometry.

The logic of class assigning is based on comparing the partial concentrations; the SoD with the highest partial ice concentration becomes the ice type. Polygons with total ice concentration lower than 15% are discarded because it has been reported that the ice edge determined from passive radiometer using 15% concentration matches best the ice edge determined from SAR data [9]. Although the WMO standards defines 15 ice classes by different SoD codes, we use only five classes (Open water, Nilas, Young ice, First-year ice, and Old ice) as being used in the AARI ice charts. Each ice chart has the dates of validity of information, which are typically three days backward including the date of publication for the AARI ice chart. Thus, the ice charts should be reprojected into the SAR geometries of which image acquisition time is in the valid time window.

3.2. SAR processing

After the noise correction using the methods in [4,5], the angular dependencies of sigma nought for sea ice [10] are compensated by subtracting the empirically determined slopes of -0.24 and -0.07 dB/ $^{\circ}$ for HH and HV polarizations, respectively. The incidence angle of 34.5° at swath center was used as a reference angle so that the sigma nought variations are corrected to this angle. Then each of the images is processed into the Haralick texture features [11] and the CV (coefficient of variances; i.e., the ratio of standard deviation to the mean) which are known to be useful for image segmentation problems. We used a sliding window of 25 by 25 pixels so that the pixel spacing of the texture features is equal to 1 km, resulting that each image has approximately 400 by 400 pixels. In order to capture textures in various

spatial scales, we calculated grey-level co-occurrence matrixes (GLCMs) for multiple co-occurrence distances from 1 to 12 pixels and then took the averaged GLCM to convert them into the 13 Haralick features per each polarization channel. Together with CV, the two polarization images are processed into 28 features.

3.3. Classifier training

Once pairs of rasterized ice chart and texture features are set, they are joined to train a classifier using Random Forest method [12] with the Scikit-learn [13] implementation. Hyperparameters are determined from 85% threshold of the maximum values of the fitted curves to the grid search results to avoid overfitting. It is important to note that not all samples in the rasterized ice charts are qualified for feeding because small-sized features are not present in the ice chart. For example, refrozen smooth ices between old ice floes have very different textures from the surrounding ices while such local features are not annotated in the ice chart. Thus, it is necessary to exclude such samples by filtering outliers in each ice class using class mean and standard deviation. Another concern is that since there is certain time difference between each image acquisition time and the ice charting time, the boundaries between different ice classes does not match perfectly. To minimize such mismatch, we used only samples away from polygon boundaries by more than 3 pixels, which is equivalent to 3 km in space.

4. PRELIMINARY RESULTS

For training a classifier, it is important to feed good samples to a decision model. Since SAR image itself is one of the sources of ice charting at ice service facilities, some images visually match with the reprojected ice charts quite well. From the dataset described in Section 2.2, we selected 81 images that acquired roughly even in time and space. In total of 10,310,655 non-land pixels were split into training and test dataset with a ratio of 7:3. For hyperparameter optimization of the Random Forest classifier, number of trees, number of maximum depth of the tree, and maximum number of features are tested and tuned as 11, 9, and 9 in our case. The processing time was approximately 15 minutes per scene with a single CPU core and 8 GB RAM, but the same processes for multiple scenes are easily parallelizable as long as the computation source is available.

Table I shows a normalized confusion matrix evaluated using the test dataset. As a quick feasibility test for application, 25 scenes acquired for three consecutive days were used for evaluating the trained classifier. Fig. 2 shows the mean of the HH- and HV-polarization mosaic images. Note that visual interpretability of ice/water discrimination is better in HV-polarization except for nilas which appears very dark in both polarization channel images. Fig. 3 compares the mosaic of SAR classification results with the AARI ice chart. The overall pattern of the classification result looks similar to the reference ice chart. Comparing the normalized confusion matrix in Table II with the one from the test set as in Table I,

TABLE I. NORMALIZED CONFUSION MATRIX FOR TEST DATASET

$\kappa = 0.737$		Predicted class				
		OW	N	YI	FYI	OI
Actual class	OW	0.962	0.017	0.011	0.008	0.001
	N	0.058	0.874	0.042	0.015	0.008
	YI	0.076	0.040	0.702	0.102	0.077
	FYI	0.021	0.017	0.111	0.679	0.169
OI	0.002	0.004	0.089	0.143	0.760	

OW: open water; N: nilas; YI: young ice; FYI: first-year ice; OI: old ice

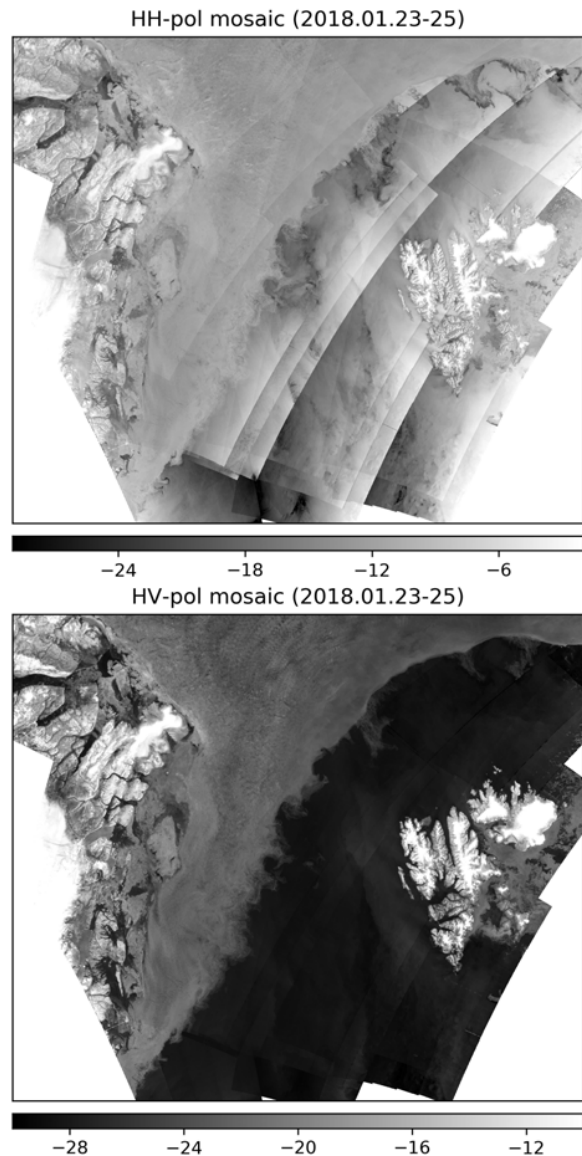


Fig. 2. Mean of the (top) HH- and (bottom) HV-polarization mosaic images. The values in the color bar indicate sigma nought.

the accuracies for open water and old ice are maintained while those for nilas, young ice, and first-year ice are slightly worse.

TABLE II. NORMALIZED CONFUSION MATRIX FOR DATA IN FIG.3

$\kappa = 0.663$		Predicted class				
		OW	N	YI	FYI	OI
Actual class	OW	0.955	0.038	0.005	0.001	0.001
	N	0.592	0.301	0.090	0.013	0.001
	YI	0.144	0.205	0.547	0.090	0.012
	FYI	0.009	0.003	0.297	0.479	0.210
	OI	0.005	0.001	0.039	0.210	0.743

OW: open water; N: nilas; YI: young ice; FYI: first-year ice; OI: old ice

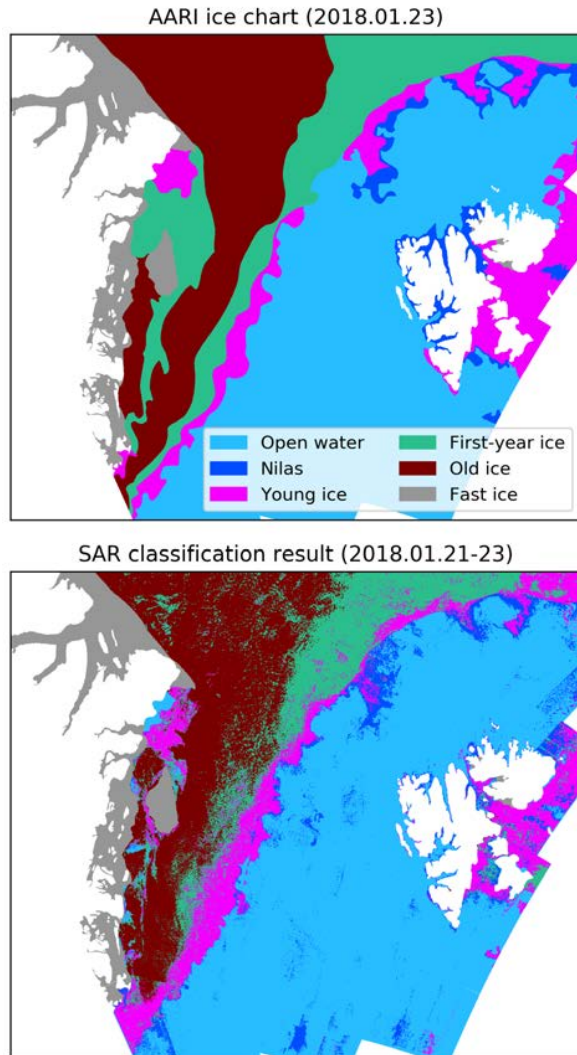


Fig. 3. Comparison between (top) the AARI ice chart and (bottom) the SAR classification result. The fast ice coverage in the SAR classification result is copied from the AARI ice chart.

5. DISCUSSION AND CONCLUSIONS

The discrimination between open water and ice seems to be possible with very high accuracy (>95%) but the separability among the ice types except old ice is rather problematic (<60%) compared to those reported in the previous works (>80%) based on RADARSAT-2 [2] or ENVISAT ASAR

[14]. This is partly because there is always differences in time and resolution between the reference ice charts and the SAR acquisitions, while a manual scene-to-scene interpretations were used as reference in the conventional works.

To the best of our knowledge, this is the first time to use the operational ice chart directly for training a classifier without any manual work. Considering the fact that the ice chart does not include small features, the accuracy acquired in this study is thought to be negatively biased. Based on the preliminary results, it is promising that a fully automated algorithm actually can work for generating ice chart-like map interpretation in a systematic way. Further investigation with more extensive data will be added in order to evaluate the performance of the proposed method.

REFERENCES

- [1] S. Leigh, Z. Wang, and D. A. Clausi, "Automated ice-water classification using dual polarization SAR satellite imagery," *IEEE Trans. Geosci. Remote Sens.*, vol. 52, no. 9, pp. 5529-5539, Sep. 2014.
- [2] H. Liu, H. Guo, and L. Zhang, "SVM-based sea ice classification using textural features and concentration from RADARSAT-2 dual-pol ScanSAR data," *IEEE J. Sel. Top. Appl. Earth Obs. Remote Sens.*, vol. 8, no. 4, pp. 1601-1613, Apr. 2015.
- [3] N. Zakhvatkina, A. Korosov, S. Muckenhuber, S. Sandven, and M. Babiker, "Operational algorithm for ice-water classification on dual-polarized RADARSAT-2 images," *Cryosphere*, vol. 11, pp. 33-46, 2017.
- [4] J.-W. Park, A. Korosov, M. Babiker, S. Sandven, and J.-S. Won, "Efficient thermal noise removal for Sentinel-1 TOPSAR cross-polarization channel," *IEEE Trans. Geosci. Remote Sens.*, vol. 56, no. 3, pp. 1555-1565, Mar. 2018.
- [5] J.-W. Park, J.-S. Won, A. Korosov, M. Babiker, and N. Miranda, "Textural noise correction for Sentinel-1 TOPSAR cross-polarization channel images," *IEEE Trans. Geosci. Remote Sens.*, Accepted for publication.
- [6] W. Tan, J. Li, L. Xu, and M. A. Chapman, "Semiautomated segmentation of Sentinel-1 SAR imagery for mapping sea ice in Labrador coast," *IEEE J. Sel. Top. Appl. Earth Obs. Remote Sens.*, vol. 11, no. 5, pp. 1419-1432, May 2018.
- [7] D.-B. Hong and C.-S. Yang, "Automatic discrimination approach of sea ice in the Arctic Ocean using Sentinel-1 Extra Wide Swath dual-polarized SAR data," *Int. J. Remote Sens.*, vol. 39, no. 13, pp. 4469-4483, May 2018.
- [8] International Ice Charting Working Group, "SIGRID-3: A vector archive format for sea ice charts," *JCOMM Technical Report Series No. 23*, WMO/TD-No. 1214, 2004.
- [9] J.F. Heinrichs, D.J. Cavalieri, and T. Markus, "Assessment of the AMSR-E sea ice concentration product at the ice edge using RADARSAT-1 and MODIS imagery," *IEEE Trans. Geosci. Remote Sens.*, vol. 44, no. 11, pp. 3070-3080, Nov. 2006.
- [10] M. Mäkynen and J. Karvonen, "Incidence angle dependence of first-year sea ice backscattering coefficient in Sentinel-1 SAR imagery over the Kara Sea," *IEEE Trans. Geosci. Remote Sens.*, vol. 55, no. 11, pp. 6170-6181, Nov. 2017.
- [11] R.M. Haralick, K. Shanmugam, and I. Dinstein, "Textural features for image classification," *IEEE Trans. Syst. Man. Cyb.*, vol. SMC-3, no. 6, pp. 610-621, Nov. 1973.
- [12] T.K. Ho, "The random subspace method for constructing decision forests," *IEEE Trans. Pattern Anal. Mach. Intell.*, vol. 20, no. 8, pp. 832-844, Aug 1998.
- [13] Pedregosa et al., "Scikit-learn: Machine learning in Python," *J. Mach. Learn. Res.*, vol. 12, pp. 2825-2830, 2011.
- [14] N. Zakhvatkina, V. Alexandrov, O.M. Johannessen, S. Sandven, and I. Frolov, "Classification of sea ice types in ENVISAT synthetic aperture radar images," *IEEE Trans. Geosci. Remote Sens.*, vol. 51, no. 5, pp. 2587-2600, May 2018.